Available online at www.sciencedirect.com
SCIENCE DIRECT®
International Journal of Multiphase Flow 30 (2004) 1389–1417
International Journal of Multiphase Flow
www.elsevier.com/locate/ijmulflow

Mechanisms for selective radial dispersion of microparticles in the transitional region of a confined turbulent round jet

Fabio Sbrizzai [a], Roberto Verzicco [b], Marco F. Pidria [c], Alfredo Soldati [d,*]

[a] *Dipartimento di Energetica e Macchine, Università degli Studi di Udine, 33100 Udine, Italy*
[b] *Dipartimento di Ingegneria Meccanica e Gestionale and Centre of Excellence for Computational Mechanics (CEMeC), Politecnico di Bari, 70125 Bari, Italy*
[c] *Advanced Process Technologies, Centro Ricerche Fiat (CRF), Strada Torino, 50-10043 Orbassano (TO), Italy*
[d] *Centro Interdipartimentale di Fluidodinamica e Idraulica and Dipartimento di Energetica e Macchine, Università degli Studi di Udine, 33100 Udine, Italy*

Received 29 February 2004; received in revised form 12 July 2004

Abstract

The dispersion of particles of different diameters in a confined turbulent round jet is dominated by the local interactions between dispersed phase and large-scale, time dependent flow structures which populate the near-field of the jet. In this work, we address first the problem of identifying the flow structures which form in a three-dimensional, turbulent confined round jet, considering also the influence of the solid walls. Second, we examine particle dispersion specifically focusing on their preferential distribution. The three-dimensional, time dependent flow field is calculated using a finite-difference LES solver of the Navier–Stokes equations in a cylindrical reference frame, whereas the dispersion of particles is computed using a one-way coupling Lagrangian approach. The flow field is characterized by mutually interacting, transitional structures of different temporal and spatial scales. We investigate the behavior of particles, in turn characterized by different size and time-scales, with the object of examining their selective response to the various scales of the flow. Our analyses confirm that multiple organized structures grow up following different types of instability, and successively interact, creating the conditions for the developing of a three-dimensional vorticity field downstream the near-field of the jet. We show that the vortical structures interact selectively with the different size particles, producing different distribution patterns and dispersion rates

* Corresponding author. Tel.: +39 432 558020; fax: +39 0432 558027.
E-mail address: soldati@uniud.it (A. Soldati).

0301-9322/$ - see front matter
doi:10.1016/j.ijmultiphaseflow.2004.07.004

qualitatively depending on the particle-to-fluid Stokes number. Following the model proposed previously, we complete the description of the particle dispersion mechanism based on the action of the large spanwise vortices, evidencing the effect of the secondary structures (ribs) on the smaller particles. We characterize the different distribution pattern of particle swarms and we analyze from a qualitative viewpoint particle dispersion behavior with the dynamics of the different transitional structures providing guidelines for dispersion control.

Keywords: Round jet; Kelvin–Helmholtz instability; Segregation; Eulerian–Lagrangian approach

1. Introduction

Large-angle axisymmetric diffusers are used to connect pipes of different diameter in many industrial applications, including transport systems, ducts and hydraulic plants. When passing through the diffuser, the flow separates from the wall immediately at the expansion and adjusts to the downstream diameter according to the dynamics of a confined round jet. In the case of multiphase flows (oil lines, smoke exhaust systems, combustion devices), phase distribution and mixing are influenced strongly by the dynamics of the flow field (Hussain and Clark, 1981), and in the specific case of a flowing gas with entrained particles, the transitional structures, which develop from the instability waves creating the flow in the diffuser (Hussain, 1986; Bernal and Roshko, 1986) control local particle dispersion and in turn the overall efficiency of the device. For instance, non-uniform particle distribution can severely downgrade the efficiency of post-treatment devices and particulate filters as those used in diesel exhaust engine systems. This specific application is the motivation of the present study.

In this work, we study the behavior of a jet surrounded by a large-angle diffuser focusing on the interactions between the coherent structures which form in the near-field and the dispersion of microparticles. Our object is to identify the structures which are specifically responsible for particle segregation and mixing at the same time providing quantitative measures of particle non-uniform distribution. Identifying the mechanisms leading to particle segregation may contribute to define methodologies suitable to increase dispersion homogeneity, for instance, by controlling the characteristic scales of specific, geometry-dependent flow structures. We want to remark here that in cases where chemical reactions among flowing gases and suspended matter occur, as in the case of diesel post-treatment systems, driving the present work, a first crucial step is to know velocity and local position of the dispersed species to control the overall throughput of the device.

It is known that dispersion of inertial particles can be dominated by flow structures which may also induce segregation, and we aim our focus to structures larger than the smallest, non-coherent, turbulent scales. These large-scale structures show spatial and temporal coherence, and control the motion of inertial particles in a variety of turbulent flows, from homogeneous turbulence (Eaton and Fessler, 1994), to boundary-layer turbulence (Marchioli and Soldati, 2002; Marchioli et al., 2003), and to turbulent jets (Tang et al., 1992). Observations confirm that all the structures examined in this work form as a result of the instabilities of initially laminar shear layers (or boundary layers) as well as of turbulent ones (Hussain, 1986).

The flow structures observed in this specific confined, round jet span over a specific range of spatial and temporal scales and show a configuration similar to those observed in plane free jets, separated boundary-layers and round free jets which have been the object of a large number of works. In particular, Yule (1978) identified experimentally the main transitional structures generating from the axisymmetric shear-layer, focusing on their spatio-temporal evolution and on their decay to turbulence by three-dimensionalization of the vorticity field (Hussain, 1986). More recently, Na and Moin (1998) used direct numerical simulation to investigate the generation mechanisms of coherent structures in separated boundary-layers, whereas Stanley et al. (2002) and da Silva and Métais (2002), focused on planar jets. Other authors (Kaltenbach et al., 1999), address specifically to diffusers, focusing preferentially on the time-averaged features rather than on instantaneous flow structures.

In his work, Yule (1978) made a distinction between two regions downstream the boundary-layer separation; the *transitional flow* region, immediately downstream the boundary-layer separation, where transitional (i.e. not yet turbulent) structures are clearly identifiable as large-scale motions, and the *turbulent flow* region, further downstream, where structures lose coherence and non-coherent three-dimensional vorticity regions (*eddies*) are formed. Our analysis is focused on the transitional-flow region, where particle dispersion is initially determined.

Particle dispersion was studied in axisymmetric jets by Chung and Troutt (1988), Longmire and Eaton (1992) and Anderson and Longmire (1995), among others, in coaxial jets by Apte et al. (2003) and in plane mixing layers by Chein and Chung (1988), Crowe et al. (1989), Wen et al. (1992), Marcu and Meiburg (1996), Yang et al. (2000), among others. These studies have shown that the large-scale flow structures which form in shear-layers play a major role in the dispersion processes because they generate preferentially directed, non-random motion of particles leading to preferential concentrations. Understanding the relationships between fluid dynamics and particle preferential distribution may provide a tool to control the instantaneous particle concentration field.

In particle-laden flows, the key parameter controlling dispersion is the ratio between the particle aerodynamic response-time and the relevant flow time-scale, known as the Stokes number, St (Crowe et al., 1989). In particular, previous studies (Crowe et al., 1989; Chung and Troutt, 1988; Ahmed and Elghobashi, 2001, among others) remark that the strongest interaction—e.g. the interaction leading to preferential distribution—is found for particles and structures having similar timescales (i.e. for $St \sim 1$).

Literature review underlines that extensive studies on particle dispersion in the round jet configuration are still lacking, and we could not find studies in which dispersion of inertial particles was examined in connection with the time-dependent dynamics of the flow structures of the confined, round jet.

In this work, we will focus on the case of an idealized diesel exhaust system and we will use a finite-difference LES solver of the Navier–Stokes equations, written in cylindrical coordinates, to simulate the flow field of the diffuser confined-jet, and a Lagrangian tracking algorithm to investigate the dispersion mechanisms of inertial particles. Our first aim is to try to clarify the mechanisms controlling the formation of the geometry dependent azimuthal and streamwise coherent structures in the transitional flow region of a circular bounded-jet developing in an expansion. Our second aim is to describe both from a qualitative and quantitative viewpoint the effects of the interactions between the dynamics of particles and that of the examined transitional structures, by characterizing the behavior of inertial particles with different response time.

In particular, we will focus on the mechanisms driving particle dispersion in the outer region of the jet—i.e. the region outside the Kelvin–Helmholtz rollers. In their work, Longmire and Eaton (1992) have shown that particle dispersion is caused by the mutual interaction between Kelvin–Helmholtz rollers and particle inertia. In this work, we pinpoint the role of the secondary structures, characterized by streamwise vorticity, in driving particles in the outer region.

2. Methodology

2.1. Computational domain and flow parameters

Fig. 1 shows a schematics of the computational domain for the axisymmetric bounded-jet. The flow parameters are those of an exhaust gas produced by a turbocharged, internal-combustion engine at 600 K ($\nu = 1.57 \times 10^{-5}$ m^2/s, $\rho = 0.965$ kg/m^3). We remark here that our aim is not to simulate an actual, detailed configuration characterized by flow pulsations and specific design geometry. Rather, our aim is to simulate a general configuration to achieve specific understanding on particle interactions with the transitional geometry-dependent flow structures. Thus, we assume that the flow is ideally steady and enters the domain from the smaller duct on the left (referred to as *inlet-pipe* henceforth) with a fully-developed velocity profile having mean velocity (*bulk velocity*) $U_b = 5$ m/s, corresponding to a bulk Reynolds number $Re_b = 2U_b \cdot r_m/\nu = 17\,516$. The inlet, time-average velocity profile corresponds to a turbulent profile with shear Reynolds number $Re^* = u_\tau r_m/\nu = 470$.

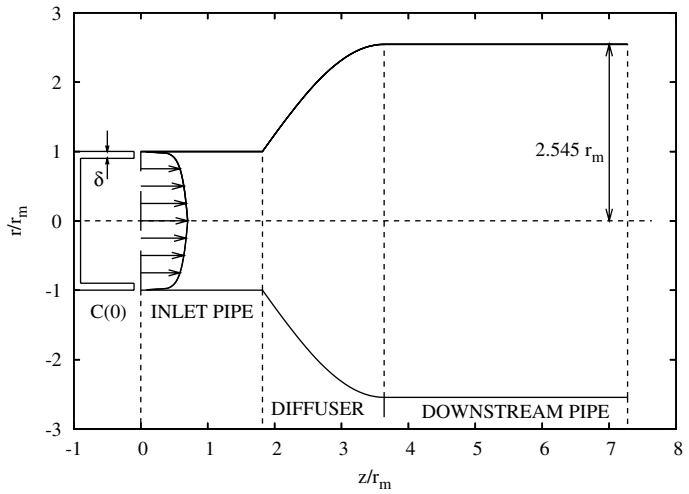

Fig. 1. Dimensions and shape of the computational domain (cross section). A turbulent, time-averaged velocity profile with shear Reynolds number of 470 is imposed at inlet. Initial particle distribution $C(0)$ is also shown: 50% of particles used in Lagrangian tracking is initially concentrated inside the boundary-layer, in a layer $\delta = 10$ wall units thick. Reference frame is cylindrical, with origin on the symmetry axis ($z = 0$, $r = 0$). Third dimension is the rotation angle around the symmetry axis θ, not shown here.

The reference coordinate system is cylindrical with θ, r and z representing azimuthal, radial and axial directions, respectively. The origin of the coordinate system is located at the center of the upstream boundary of the inlet-pipe (see Fig. 1).

All quantities are made dimensionless using the inlet-pipe radius r_m (2.75×10^{-2} m) as a reference length-scale, the bulk velocity U_b as a reference velocity and the following reference time:

$$\tau = \frac{r_m}{U_b} = 5.5 \times 10^{-3} \text{ s}. \tag{1}$$

As shown in Fig. 1, the geometry is made by the *inlet-pipe*, from $z = 0$ to $z = 1.818 r_m$, with radius equal to r_m; the *diffuser*, from $z = 1.818 r_m$ to $3.636 r_m$, the shape of which is defined through the following function $r(z)$:

$$\frac{r}{r_m} = 1 + \left(\frac{D}{2r_m} - 1\right) \cdot \sin\left[\left(\frac{\pi}{2}\right)\frac{z - L}{L}\right] \tag{2}$$

with $D = 5.09 r_m$ being the maximum diameter of the diffuser and $L = 1.818 r_m$ the inlet-pipe length; and the *downstream-pipe* (as it will be referred hereinafter), with diameter D, and extending from $z = 3.636 r_m$ to $z = 7.273 r_m$. The overall length of the domain is thus $7.273 r_m$.

At the inlet boundary we apply an axisymmetric, analytical velocity profile, equal to the time-averaged turbulent velocity profile calculated for a shear Reynolds number $Re^* = 470$ using the logarithmic approximation: $u_z^+ = 2.5 \ln(r_m - r)^+ + 5.5$. As specified earlier, the average velocity for this profile equals to $U_b = 5$ m/s and no turbulent fluctuations are imposed. At the outlet boundary we apply the following convective condition

$$\frac{\partial u_z}{\partial t} + U_c \frac{\partial u_z}{\partial z} = 0, \tag{3}$$

which allows the non-stationary structures advected by the main flow to leave the computational domain without being reflected (Lowery and Reynolds, 1986; Pauley et al., 1988; Na and Moin, 1998; Kaltenbach et al., 1999). U_c is set equal to the mean streamwise velocity

$$U_c = \frac{4}{\pi D^2} \int_0^{2\pi} \int_0^{\frac{D}{2}} u_z r \, d\theta \, dr, \tag{4}$$

which works optimally for a turbulent flow (Le et al., 1997).

Calculations started from a still-fluid initial-condition, in which the inlet velocity profile is progressively increased from zero to its final value up to the time of 9.09τ. Then, the simulation proceeded up to 68.55τ to achieve statistical convergence, i.e. stabilization of the overall quantities (kinetic energy and momentum rate) and of the periodicity of large-scale motions associated to the transitional-flow structures. From this point onward, we started to save the flow field database for a time-window of 31.21τ (up to 99.76τ) corresponding to 4.293 times the through-flow period.

2.2. LES solver

Mass and momentum balance (Navier–Stokes) equations are solved in a cylindrical reference frame by means of the finite-difference, large-eddy simulation code described in Verzicco and Orlandi (1996). The code solves for the Navier–Stokes equations on a staggered grid for velocity and

pressure and uses a fractional-step with approximate factorization second-order accurate technique in time and space. The following flow variables: $q_\theta = u_\theta$, $q_r = r \cdot u_r$ and $q_z = u_z$ and the pressure p, obtained from the velocity components u_θ, u_r and u_z (i.e. the azimuthal, radial and axial, respectively) are used in place of the velocity components to eliminate the problem associated with the singularity at $r = 0$, since q_r is identically zero (and not indetermined, as u_r would be) at $r = 0$ (Verzicco and Orlandi, 1996).

We use a resolution providing a grid point distribution uniform along θ and z coordinates, but stretched in the radial direction, with higher resolution around the shear-layer region ($r/r_m \sim 1$). The number of grid points is $257 \times 47 \times 117$ in the azimuthal, radial and axial directions respectively. To ensure grid-independent results, we performed a series of test simulations based on previous works (Akselvoll and Moin, 1996; Apte et al., 2003). The resolution we use is the result of several preliminary tests, using a grid with even 80% more points in the streamwise and radial directions. The resolution of the time-dependent structures did not show significant difference on the two grids. Current resolution compares well with recent works on similar geometries (Akselvoll and Moin, 1996; Apte et al., 2003). A posteriori analysis confirmed that the smaller structures (i.e. the smaller rib vortices) cover at least 15 grid points in the transverse direction (i.e. along the diameter), using the present configuration.

Since the code solves for the Navier–Stokes equations in a cylindrical geometry with constant radius, we chose to exploit the immersed-boundaries method described in Fadlun et al. (2000) to model the no-slip and no-cross boundary conditions applied to all the solid boundaries. This approach is widely used to model the complex-shape domains on structured grids and we found it useful to simulate the present geometry, characterized by sudden diameter variations. To account for the subgrid turbulent scales (SGS) the model described in Germano et al. (1991) has been used. In Verzicco et al. (2000) more details on the implementation of the SGS model in the cylindrical coordinate code and its suitability to the immersed boundary method are discussed in detail.

2.3. Choice of inlet conditions

We considered carefully the problem of inlet conditions. In our work, the reference geometry is a diffuser preceeded by a long, straight pipe in which the flow is steady. This is an 'idealized' representation of a turbocharged diesel exhaust engine. Our aim is to study the influence of flow structures on the dispersion of particles which are small but characterized by a time scale larger than the turbulent flow scales which are not directly caused by the exit geometry. We believe that, in the inertial range examined, particle outward dispersion in the near field of the confined jet is dominated by the large-scale, geometry-dependent flow structures and is only scarcely affected by the turbulence fluctuations. This will be confirmed a posteriori.

We examined in detail what recent works have shown as per as the influence of the inlet conditions. Lee et al. (1992) simulated the influence of inlet turbulence on spatially evolving flows superimposing to the mean inlet profile stochastic perturbations with a carefully prescribed spectrum. Akselvoll and Moin (1996) in confined, coannular round jets and Na and Moin (1998) in a backward facing step used inlet profiles calculated by an independent pipe (Akselvoll and Moin, 1996) and channel (Na and Moin, 1998) periodic flow simulation. To the best of our knowledge, there is only one simulation (Kaltenbach et al., 1999) in which a domain large enough to allow steady state turbulent channel flow at the diffuser inlet is adopted. In their work, Kaltenbach

et al. (1999) observe that accurate inlet conditions are crucial for the correct calculation of the flow structures in the diffuser. However, they simulate a mild slope diffuser with weak or absent separation in which the geometry-induced perturbations play a role which is not at all dominant compared to that played by the evolution of the flow structures exiting the channel.

Therefore, considering first that the flow dynamics in the transitional region in the present study is influenced strongly by the discontinuity of the geometry and very weakly by the inlet turbulence (Hussain, 1986); Considering further that simulating accurately inlet turbulent conditions (Kaltenbach et al., 1999) would increase the computational cost of the simulation more than 10 times and finally, observing that including artificial inlet conditions (Na and Moin, 1998; Akselvoll and Moin, 1996; Le et al., 1997) would represent an additional source of uncertainty in our simulations we decided to neglect turbulence fluctuations in our inlet section.

A posteriori analysis of our results showed that the position of the first Kelvin–Helmholtz roll up coincides with that shown e.g. by Longmire and Eaton (1992), and is placed at about $x/D \cong 1$.

2.4. Lagrangian tracking

Once we obtained a fully developed flow, we simulated the behavior of 4×10^4 flyashes particles, with density $\rho_p = 1000\,\mathrm{kg/m^3}$. We expect that particles of different diameter will interact selectively with the coherent structures, depending on their Stokes number (Chung and Troutt, 1988; Ahmed and Elghobashi, 2001), and for this reason we chose to simulate particle diameters from 10 to 100 μm for which the dimensionless characteristic time $\tau_p^* = \rho_p d_p^2/(18\mu\tau)$ varies from $6.67 \times 10^{-2}\tau$ to 6.67τ. The large-scale flow structures time-scales show values for which the Stokes number is in the range $O(10^{-2})$ to $O(10^{1})$. These values were calculated a posteriori, post-processing the flow simulation. Details on particle characteristics and Stokes numbers are reported in Table 1.

We calculate the trajectory of each particle by integrating explicitly over time the equation of motion. The assumptions for particle modeling are: (i) all particles are non-interacting non-deformable solid spheres; (ii) particle density is large if compared to fluid density; (iii) the effect of the particles on the flow is neglected. According to many previous works (see, for instance, Chung and Troutt, 1988; Loth, 2000; Armenio and Fiorotto, 2001), the study of the order of magnitude of the forces acting on particles based on the work by Maxey and Riley (1983) reveals that the drag force is $O(St^{-1})$, the virtual mass and the pressure gradient are $O(\rho/\rho_p)$ and the Basset force is $O((\rho/\rho_p)^{1/2})$. In our work, $\rho/\rho_p = O(10^{-3})$ and St based on the reference timescale for the fluid (see Table 1) is in the range $[10^{-2}$–$10^{1}]$. In the current work, the effect of the Saffman force

Table 1
Particle sizes, characteristic time-scales and Stokes numbers used for Lagrangian tracking

d_p [μm]	τ_p [τ]	St_{VR}	St_r
10	6.67×10^{-2}	4×10^{-2}	6.67×10^{-2}–2.68×10^{-1}
20	2.68×10^{-1}	0.16	2.68×10^{-1}–1.062
50	1.667	0.988	1.68–6.72
100	6.67	3.95	6.72–26.88

Two Stokes number are reported for each particle diameter, referred respectively to the vortex-ring turnover time ($St|_{\mathrm{VR}}$) and to the rib turnover time ($St|_r$).

is negligible. The ratio between Saffman force and the Stokes drag is $O(d_p^2\sqrt{\mathrm{d}u/\mathrm{d}y}/v)$ and, for particles with small diameter and low inertia this force is negligible with respect to drag force (Apte et al., 2003; Crowe et al., 1998). Finally, following the assumption of Chung and Troutt (1988), for the range of Stokes number examined here, we can assume that gravity force is negligible, since it gives a maximum contribute of some percent for the larger 100 μm particles (Chung and Troutt, 1988). The equation of motion reduces thus to a balance of Stokes drag and particle inertia:

$$\frac{\mathrm{d}v_i}{\mathrm{d}t} = \alpha\{u_i[x_j(t), t] - v_i(t)\}, \tag{5}$$

where $x_j(t)$ and $v_i(t)$ are particle position and velocity at t, u_i are the fluid velocity components at $\vec{x}(t)$ and α is the inverse of the particle response time:

$$\alpha = \frac{1}{\tau_p} = \frac{18\mu}{\rho_p d_p^2}, \tag{6}$$

which involves the following expression for the drag coefficient: $C_\mathrm{D} = 24/Re$. This expression for the drag coefficient is valid for $Re_p = O(1)$, Re_p being the particle Reynolds number, i.e.:

$$Re_p = \frac{d_p \mid \vec{u} - \vec{v} \mid}{v}. \tag{7}$$

We use the Stokes coefficient for drag, with the following non-linear correction (Rowe and Enwood, 1962) when $Re_p > 1$:

$$C_\mathrm{D}(Re_p) = \frac{24}{Re_p}(1 + 0.15Re_p^{0.687}), \tag{8}$$

which is a good approximation up to $Re_p = 10^3$. We verified a posteriori that particle Reynolds numbers never exceed this limit.

The drag force is evaluated by calculating the fluid velocity $\vec{u}$ at each particle position using a trilinear interpolation of the velocity value at cell centers. For the technical details regarding particle tracking on a cylindrical coordinate system, which presents a strong influence of the numerical singularity along the pipe axis, we refer to the previous works by Cerbelli et al. (2001) and Marchioli et al. (2003).

When using LES to predict particle behavior, particle equation of motion should include an SGS model to account for the non-resolved sub-grid scales or, if such a model is not exploited, it has to be verified that particle dispersion is not affected by these scales. Following the assumptions of Apte et al. (2003), direct effect of the SGS fluctuations on particle dispersion has been neglected. Indeed, the direct effect of the sub-grid scales is expected to be important when the sub-grid scale energy is significant (compared to the resolved scales) and the SGS fluctuation timescale is comparable to the particle relaxation time (i.e. for $\tau_p/\tau_\mathrm{SGS} = O(1)$). In the present case, we ensured that the smaller scales able to affect particle motion (i.e. for which $St \sim 1$) are explicitly resolved by the code. Discussion on this point follows.

We start from the assumption that the smallest scales explicitly resolved by a LES code with a given grid spacing have the same spatial scale, velocity scale and time scales of the inertial range. If Δ represents the grid spacing and τ_d the characteristic timescale of the structure with dimensions equal to Δ; it results:

$$\tau_d = T\left(\frac{\Delta}{L}\right)^{2/3}, \tag{9}$$

where L and T are respectively the characteristic timescale and integral length scale of energy spectrum. In the present case, grid spacing varies with $1/r$ (due to azimuthal spacing) and the most restrictive condition is at external wall, where $\Delta = \Delta_{\max} \cong 0.062 r_m$. However, in this region particle presence is not observed. The external region of the shear layer is mostly interested by particle motion and coherent structure presence. Here, grid spacing is about $\Delta = 0.04 r_m$. We took L and T equal to the scales at which energy is supplied to spectrum, i.e. the larger vortex-ring scales for which $L = r_m/3$ (i.e. the vortex-ring core diameter) and $T = \tau/3$. We obtain: $\tau_d \cong 0.081\tau$. For the smaller 10 μm particles, for which $\tau_p = 0.0667\tau$, the Stokes number is 0.827, i.e. $St = O(1)$. For this reason, we did not introduce an SGS model in particle tracking.

Particle initial velocity is set equal to the instantaneous fluid velocity at the cell location. For time-advancement, we used an explicit first-order Euler method which leads to higher position errors with respect to higher-order methods and requires very small time steps, in this case set equal to the LES code timestep. We made this choice because of the larger system memory requirements due to integration of a large number of particles.

3. Results

3.1. Mean flow field validation

As discussed in Section 1, there is virtually no previous detailed analysis of the flow field in a confined transitional round jet. We thus decided to validate our numerical results against previous data on free jets.

In Fig. 2(a) and (b), time and azimuthally averaged axial-velocity profiles are reported. The velocity field is averaged over the time-window within 68.55τ and 99.76τ, and is then averaged along the θ coordinate, obtaining the two-dimensional data we show in Fig. 2(a) for 10 different section planes at as many different z locations. We can observe that the boundary-layer separates at the point where the inlet-pipe and the diffuser join (point A). From here, a shear-layer (the external limit of which is identified by the dashed line) forms and grows downstream. A recirculation cell (i.e. negative values of the axial velocity) is observed as an effect of the presence of surrounding solid walls, in the *outer region* (namely, the region that lies outside the shear-layer limit). The reason for the presence of a recirculation here is that an excess of fluid is driven out of the domain by the jet-spreading, and must re-enter axially through the outer region.

The computed profiles are compared with the analytical jet boundary velocity profile described by Schlichting (1979), plotted in Fig. 2(a) with circular dots. We should remark here that in Schlichting (1979) the initial (nozzle) jet velocity profile is rectangular instead of the current log-law, giving place to an initially flat velocity distribution near jet centreline. Thus, in the region of the mixing layer, far from the boundaries and far from the jet exit, the agreement is good.

In Fig. 2(b) a comparison with experimental data for round jets of Davies et al. (1963) and Bradshaw et al. (1964) is presented. We compared the profiles at the axial position z_1 and z_2 indicated by arrows in Fig. 2(a). Considering that Davies et al. (1963) and Bradshaw et al. (1964)

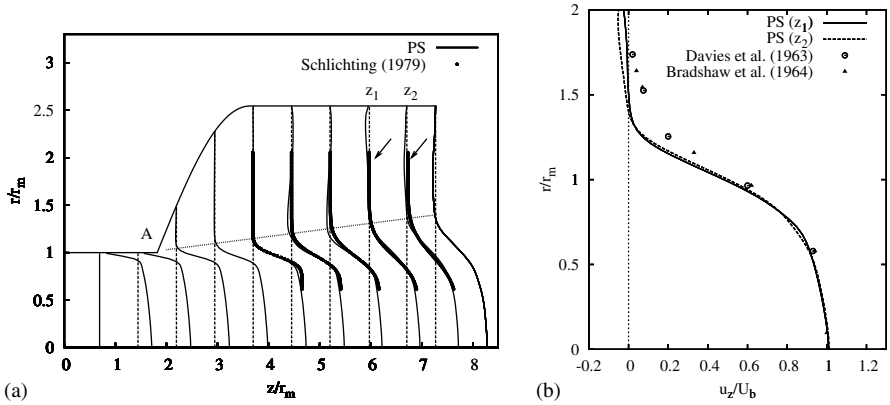

Fig. 2. Time- and θ-averaged axial velocity profiles obtained from present simulation (PS), compared with (a) the theoretical turbulent jet boundary profile described in Schlichting (1979), and (b) with the experimental data of Davies et al. (1963) and Bradshaw et al. (1964) for a circular jet. In (a), the dashed line indicates the external limit of the shear-layer, starting from the separation point A. The external limit of the shear-layer for the confined jet is not as large as that of a circular free jet, due to the presence of an external wall, which causes also a recirculation effect (small negative velocities) visible in (b) for $r/r_m \geqslant 1.5$. The two profiles used in (b) are marked with arrows in (a).

investigated a free jet issued by a nozzle, we cannot compare up to the domain boundary. We found a good agreement of our data against experiments on a free round jets up to $r/r_m \cong 1$, whereas for larger values, the recirculation effect is responsible for a sudden velocity decrease within $1 < r/r_m \leqslant 1.5$ and small negative velocities (recirculation) for $r/r_m > 1.5$.

We will discuss later comparison against experimental data of vortex-shedding frequency.

3.2. Qualitative flow field dynamics

For the purposes of the present work, it is important to describe the dynamics of the flow structures which dominate particle transport. We will describe here briefly the average features and the main structures of the flow field. The reader is referred to previous papers (Yule, 1978; Hussain and Clark, 1981; Bernal and Roshko, 1986; Chung and Troutt, 1988; da Silva and Métais, 2002; Stanley et al., 2002) in which the flow field forming in various shear layer configurations and in enlargements is studied in detail by means of various techniques.

Before describing our field observations, we want to use cartoons to elucidate some key features of the large-scale structures which we observed in the near-field of the axisymmetric shear layer (Yule, 1978; Hussain and Clark, 1981; Bernal and Roshko, 1986). Even though this mechanism may be known, we believe this description useful to describe particle dynamics in the diffuser. Fig. 3 shows a schematic representation of the transitional structures which evolve in the shear layer region of the specific round jet. A Kelvin–Helmholtz initial instability of the shear-layer near the inlet-pipe causes an intermittent aggregation of vorticity to form uniformly distributed coherent concentrations, which take the aspect of a periodic street of vortex-rings (VR), as an effect of the shear-layer rollup (Yule, 1978). Advancing downstream, the vortex ring (see the VR3 vortex in Fig. 3) loses its axial symmetry assuming an irregular (lobed) shape due to a wave-instability of its core. The wave-deformation of this vortex-ring appears together with outward *bursts* of fluid (i.e.

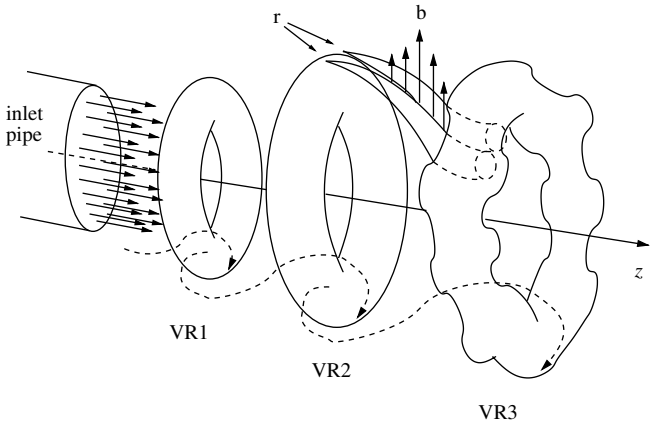

Fig. 3. Schematics of the evolution of the coherent structures in the shear-layer. Vortex-rings (VR) are shed periodically down to $2r_m$ from the inlet-pipe. Further downstream they undergo a wave-deformation associated to radial fluid-ejections (bursts—b) and streamwise vortex-pairings (ribs—r).

radial, short-lived jets directed towards the outer region) that apparently originate inbetween couples of successive Kelvin–Helmholtz billows (Yule, 1978; Hussain and Clark, 1981; Hussain, 1986). The two phenomena appear simultaneously, and we try now to give an explanation of the mechanisms leading to the formation of such structures.

The mechanisms by which the vortex rings undergo the wave deformation have been described, among others, by Klaassen and Peltier (1989). In that work, authors note that the Kelvin–Helmholtz billows of a shear layer can give rise to a spontaneous growth of longitudinal (either spanwise periodic, for plane shear layers or azimuthally periodic, for axisymmetric shear layers) convective disturbances confined to those regions of the vortex core in which the original velocity profile has been inverted by the roll-up of the billow (Klaassen and Peltier, 1989). Following the evolution of this mechanism, we observe that when the VR begins to undulate, portions of it penetrate into the potential-core of the jet, characterized by larger gradients of the axial velocity u_z. This causes the inner region of the VR to be interested by a non-uniform velocity profile, characterized by periodic peaks, an example of which is shown in Fig. 4(a). As soon as this profile wraps around the roll-up of the vortex ring, it generates a local, non-uniform velocity profile of the radial component u_r (also shown in Fig. 4(a)), in turn characterized by periodic peaks. A specific periodicity exists, consequent to the periodicity of the wave-instability of the VR, leading to a quasi-constant angular distance between a burst and the adjacents. A schematic representation of a burst is shown in Fig. 4(c). We observe that the coherence of these peaks is short-lived, but the sudden appearance and disappearance of a burst causes the formation of a couple of counter-rotating streamwise vortices—called ribs (Hussain, 1983)—on both sides, as shown in Fig. 4(c). The ribs life-time is longer than that of the burst, since the couple of ribs moves slower than the burst centerline-velocity and remains in the region between two consecutive VR for a relatively longer time, during which it is stretched along the streamwise direction, creating the conditions for a self-sustaining of the structure existence, first described by Hussain (1983, 1986) and taking the shape shown in the schematics of Fig. 3 (in which (b) identifies the burst ejection, whereas (r) identifies the local couple of ribs, formed inbetween VR2 and VR3).

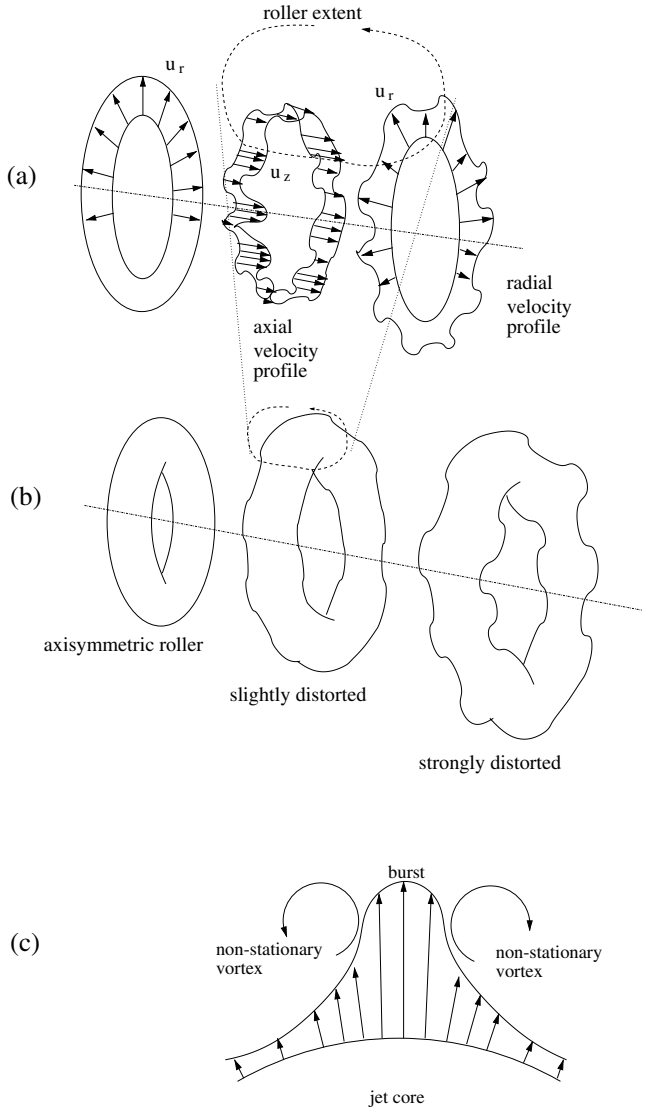

Fig. 4. Formation mechanism for the secondary radial and axial coherent structures. The vortex-ring rollup entrains a non-uniform axial-velocity profile into a non-uniform radial-velocity profile, which originates outward-directed fluid ejections (bursts). Such ejections represent a source of streamwise vorticity that develop as couples of streamwise vortices (ribs). In (c), the section of a burst with the non-stationary counter-rotating vortices originating the ribs is shown.

The transitional-flow structures described represent the first formation stages of the three-dimensional vorticity field which characterizes the turbulent flows—such as the one described by Yule (1978), developing downstream the transitional-flow region we are analyzing—where the vortex rings are replaced by non-coherent three-dimensional vorticity containing diffuse regions. Turbulent conditions are achieved when the two initially separated, orthogonal vorticities (i.e. that of the vortex ring and that of the ribs) interact (Hussain, 1986).

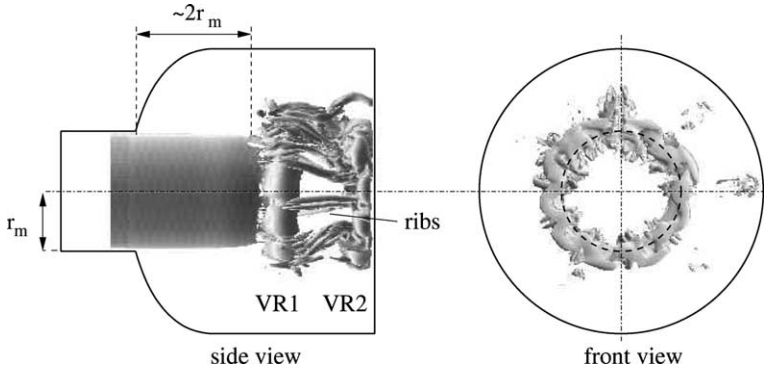

Fig. 5. Instantaneous side and front view of the vorticity magnitude isosurface $|\omega/\omega_{max}| = 0.38$ showing the vortex-ring wave-instability. Quasi-streamwise vortex pairs (ribs) are seen to connect subsequent vortex-rings (marked as VR1 and VR2 in side view). The instantaneous vorticity field is taken at $t = 68.55\tau$. Position of first roll-up apparently occurs at a distance from the inlet-pipe exit of about $2r_m$, and agrees with the experimental data of Longmire and Eaton (1992). As for the jet of Longmire and Eaton, roll-up is preceeded by a sharp interface that divides the jet flow from the surrounding fluid.

An efficient representation of the coherent VR and ribs is given through three-dimensional instantaneous vorticity isosurface visualizations. In Fig. 5, the $|\omega/\omega_{max}| = 0.38$ isosurface shows the VR and the rib structure. Here, a circular pattern of quasi-streamwise, stretched high-vorticity regions are observed to connect a pair of subsequent vortex rings showing a correspondence between the position of the rib pairs and the portions of the vortex ring which appear introflected towards the core of the jet. This correspondence is in accordance with the mechanism of rib formation described earlier, since we expect to find a burst in regions where the VR is closer to the jet core, i.e. where the higher axial velocities bend-up in the radial direction generating the burst.

3.3. Characteristics of the vortex-rings

We want to quantify the periodic behavior of the vortex-rings by calculating the frequency spectrum of the axial and radial velocity components in the shear-layer, since the passage of a VR is generally revealed by a velocity peak which should be visible for both components.

We measure velocity in two points A1 and A2, fixed in space and located into the shear-layer region ($r/r_m = 1$) at an axial position equal to $z = 5r_m$ and opposite with respect to the geometry axis ($\theta_{A1} = 0$, $\theta_{A2} = 180°$). For each point, we store the two components of the velocity field along the entire simulation time-window, obtaining two time-dependent functions for which the *coherency spectrum* can be calculated following the definition of Stanley et al. (2002), who used it to evaluate the vortex-shedding frequency in a plane shear-layer:

$$\mathrm{Coh}_{vv}(f) = \left| \int_{-\infty}^{+\infty} C_{vv}(d) \exp(-2\pi \mathrm{j} f d) \mathrm{d}d \right|. \tag{10}$$

C_{vv} is the two-time correlation $\overline{u^i_{A1}{}'(t) u^i_{A2}{}'(t+d)}$ calculated for the values measured in A1 and A2. The use of the coherency spectra reduces the influence of the broad-band background energy and stresses the discrete frequencies which are present on two arbitrary sides of the jet (Stanley et al.,

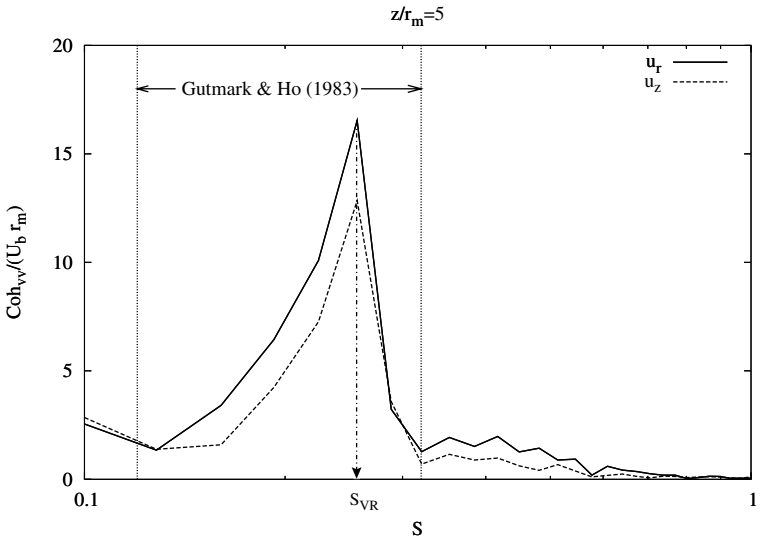

Fig. 6. Coherency spectrum of two velocity components, u_r and u_z taken in two diametrically opposite points (sensors) A1 and A2, located at $r/r_m = 1$. Spectrum is calculated with respect to the Strouhal number S. A peak is observed at $S_{VR} = 0.256$, for both components. This corresponds to the preferred mode of Kelvin–Helmholtz instability (i.e. to vortex-rings shedding frequency), measured at $z/r_m = 5$. This frequency falls within the range given by Gutmark and Ho (1983) for several jet configurations, shown here by means of the dotted vertical lines.

2002). The spectrum we obtained is shown in Fig. 6, versus the Strouhal number, we define here as $S = \tau f$, in which τ is the reference defined in Eq. (1) and f is the shedding frequency in Hz. Radial and axial velocity components exhibit a high peak for a value of S comprised between 0.2 and 0.3. The coherency spectra calculated for further seven z locations, i.e. $z/r_m = \{4, 4.25, 4.5, 4.75, 5.25, 5.5, 5.75\}$ (not shown) also give similar peaks, making it possible to identify the value of the vortex-shedding frequency in the range within $S_{min} = 0.2498$ and $S_{max} = 0.2641$.

This preferred-mode frequency has been investigated for different jet configurations in a number of works. Most of the results are collected in the work of Gutmark and Ho (1983). These authors reported, for each experiment, Reynolds and Strouhal numbers. Authors notice that Strouhal numbers vary within the range [0.24–0.64] and state that such uncertainty is attributed to low-level spatially coherent disturbances in individual facilities. Nevertheless, the value of Strouhal number we found in the present work falls within the range indicated by Gutmark and Ho (1983), as shown in Fig. 6. It has to be noticed that our values of the Strouhal number are radius-based and have to be doubled with respect to those reported by Gutmark and Ho, which are diameter-based.

The *convection velocity* of the vortex rings U_{VR}, can be determined by measuring the time required for a VR to move within two points, B1 and B2, placed in the shear layer at a fixed distance. To this aim, we measure the two velocity components u_r and u_z in the points B1 and B2, located at $\theta = 0$, $r/r_m = 1$ (inside the shear-layer) and at the axial positions z_{B1} and z_{B2}, being $z_{B1}/r_m = 4.255$ and $z_{B2}/r_m = 5.236$. The two-time correlation coefficient for B1 and B2, $C_{vv}(d) = \overline{u^i_{B1}(t) u^i_{B2}(t+d)}$—where i indicates that the ith component is considered, whereas d indicates the *delay* set between the two functions $u^i_{B1}(t)$ and $u^i_{B2}(t)$—is calculated. The result is re-

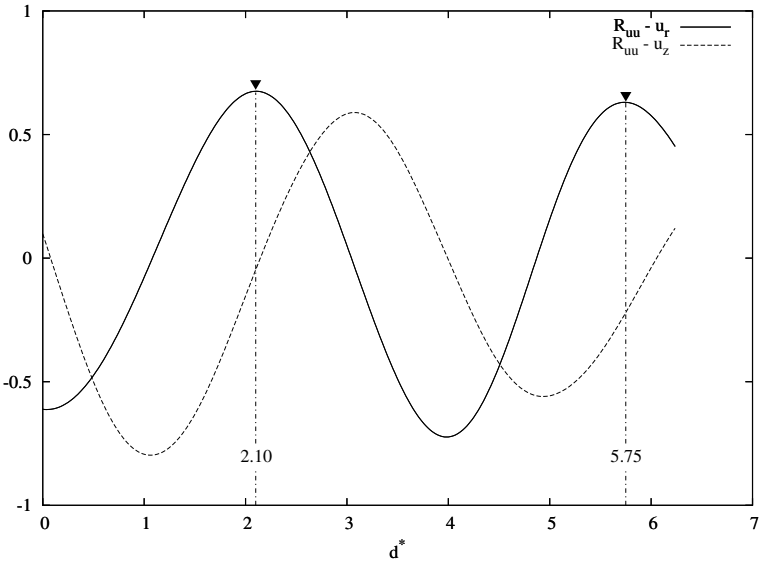

Fig. 7. Two-time correlation for the radial and axial velocity components, u_r and u_z measured in two points B1 and B2 ($z_{B1}/r_m = 4.255$, $z_{B2}/r_m = 5.236$, $\theta_{B1} = \theta_{B2} = 0°$, $r_{B1} = r_{B2} = r_m$). This correlation indicates the (non-dimensional) time required for a vortex-ring to move from B1 to B2, allowing to calculate the VR convection velocity U_{VR}.

ported in Fig. 7 for a non-dimensional delay value: $d^* = d/\tau$. We can observe two correlation maxima (see, for instance, the component u_z) located at $d^* \cong 2.10$ (first VR passage) and at $d^* \cong 5.75$. The first correlation maximum, at $d^* = 2.10$, indicates the time required for the VR to be revealed by the B2 sensor after it has been revealed by B1 (i.e. the time required for the VR to move from B1 to B2). The value of $d^* = 2.10$ indicates a convection velocity of $U_{VR} \cong 0.491 U_b$. Another measure made on a successive VR indicates a different value, of $U_{VR} \cong 0.265 U_b$. This discrepancy indicates that the VR convection velocity may vary over a certain range, even if the shedding-frequency is nearly constant.

3.4. Characteristics of bursts and ribs

In Fig. 8, an instantaneous isosurface of the second invariant of the velocity–gradient tensor (VGT), indicated as Q henceforth:

$$Q = -\frac{1}{2}\left[\frac{\partial u_i}{\partial x_j}\frac{\partial u_j}{\partial x_i}\right] = \left(\underbrace{S_{ij}S_{ij}}_{\text{STRAIN}} - \underbrace{\Omega_{ij}\Omega_{ji}}_{\text{VORTICITY}}\right), \tag{11}$$

the value of which depends on the difference between a strain term (symmetric part of the VGT) and a vorticity term (antisymmetric part of the VGT), shows the structure of a pattern of ribs. Although the number of rib couples formed inbetween two successive VR is not strictly constant, it varies over a specific range in which the value having the higher probability of occurring can be determined. To this aim, we use 120 velocity-measuring probes (indicated as Cn, n being the probe

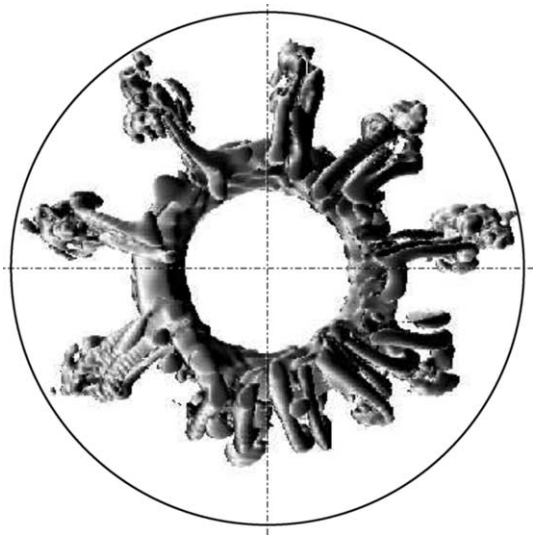

Fig. 8. Downstream view of the instantaneous $Q/Q_{\max} = 0.4$ isosurface, taken at $t = 68.55\tau$, showing the burst ejections and the rib pairs formed inbetween two consecutive vortex-rings. Q is the second-invariant of the velocity-gradient tensor (VGT).

number), located on a ring with radius $r = r_m$, which axis coincides with the domain axis, located at $z/r_m = 4.364$. The displacement between a probe and the adjacents is constant so that these are equally-spaced around the azimuthal coordinate θ. We measured the azimuthal velocity component $u_\theta(t)$ as a function of time, for all probes, storing them on as many files. The characterization of the spatial coherence for the azimuthal velocity is then carried out as follows: we choose a reference point (e.g. C1) and we calculate the cross-correlation between the value of azimuthal velocity for this point and that of all the others. The result is given as a function of the angular position θ, $C_{uu}(\theta)$, an example of which is reported in Fig. 9, for C1. As we can observe from this figure, the function $C_{uu}(\theta)$ is broadly periodic. The same procedure is adopted for other four points—C5, C10, C20 and C30—the positions of which are indicated in Fig. 9 by the vertical dash-dot lines. All these cross-correlations show a periodic-like behavior in θ, so that if a preferred azimuthal mode for the bursts can be identified, this can be done by Fourier-transforming the series of Fig. 9 into the wavenumber space ν_b:

$$C_{uu}(\nu_b) = \left| \int_{-\infty}^{-\infty} C_{uu}(\theta) \exp(-2\pi \mathrm{j} \nu_b \theta) \mathrm{d}\theta \right|. \tag{12}$$

In such a way, we obtain a wavenumber spectrum, which is useful to reveal all the specific wavenumbers associated with the preferred mode of the spatially periodic structures characterized by means of the azimuthal velocity u_θ (e.g. the ribs). The wavenumber unit found here is scaled by 2π, i.e. if a peak is observed for $\nu_b = m$, there will be m coherent events within $\theta = 0$ and $\theta = 2\pi$. Five wavenumber spectra are calculated for C1, C5, C10, C20 and C30 and are shown in Fig. 10 where a peak corresponding to $\nu_b = 8$ is visible in each spectrum, indicating that the most probable value of simultaneous bursts is, then, 8. Another high peak exists for $\nu_b = 3$, indicating that a large-scale

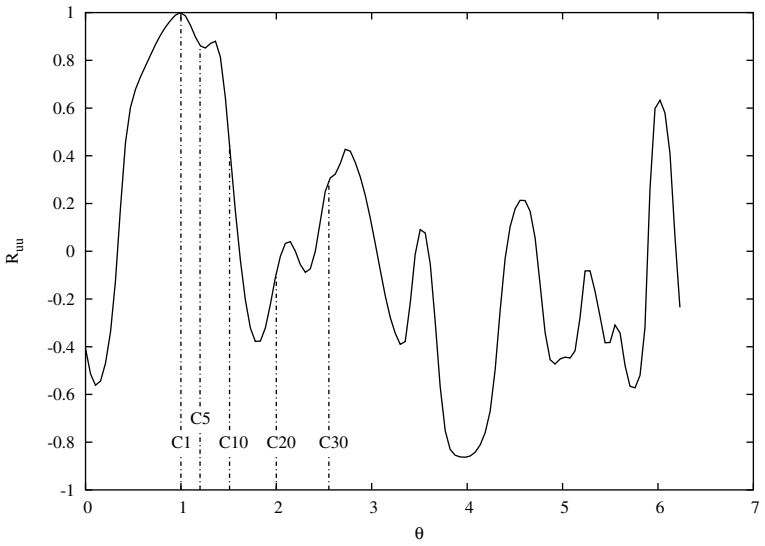

Fig. 9. Cross-correlation coefficient for the azimuthal velocity u_θ measured for $\theta_p = 1.047$ rad (point C1), and other 120 points uniformly distributed in the shear-layer, onto a ring of radius r_m, at $z/r_m = 4.364$. Here, the cross-correlation is plotted as a function of the azimuthal coordinate θ. A specific periodicity is observed, revealing that spatially periodic u_θ fluctuations, associated with the streamwise rib pairs, exist. The cross-correlation coefficient has been also calculated for the points C5, C10, C20 and C30, which position is represented by the vertical dash-dot lines.

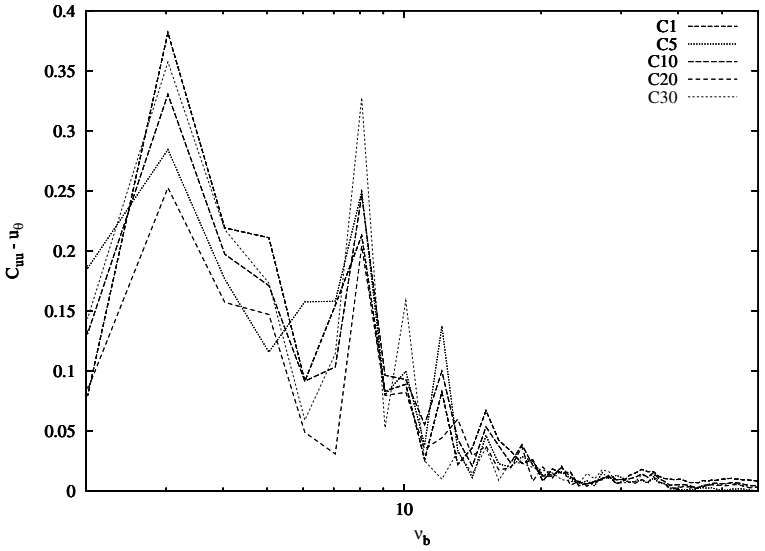

Fig. 10. Wavenumber spectrum for the azimuthal velocity component measured in the circular pattern of points C*n*. Five different spectra, corresponding to as many different reference positions (marked by C1, C5, C10, C20 and C30—see explanation in the text) are reported. Each spectrum shows a peak corresponding to the value of eight couples of ribs which represents, in a long time averaging, the most probable configuration. A peak is also observed for the value of $\nu_b = 3$, and this may indicate the presence of a large-scale periodicity (not object of the present study).

periodicity is present; this may represent some form of slow-periodic flow oscillation, the study of which lies outside the purposes of this work.

3.5. Simulation of particle dispersion

Chung and Troutt (1988), investigated numerically the interactions between inertial particles and coherent time-dependent structures of a round, free jet by issuing patterns of vortex-rings from an orifice—by means of a periodic forcing—with the assumption of inviscid flow. Although the problem described by Chung and Troutt (1988) does not include investigation of the coupling between particles and streamwise structures, their work, as well as the present, is focused on the interaction of particles with transitional structures, i.e. a class of structures including not only the vortex rings but also e.g. the ribs (Hussain, 1983; Yule, 1978). In particular, Chung and Troutt (1988) showed that particle behavior depends strongly on the ratio of particle response-time τ_p to the characteristic time of the flow structures τ_f, defined as the Stokes number, $St = \tau_p/\tau_f$. Specifically, particles with $St \ll 1$ disperse at approximately the fluid dispersion-rate, whereas particles with $St \gg 1$ disperse less than the fluid. Furthermore, the authors showed that particles with an intermediate Stokes number (i.e. $St \sim O(1)$), disperse faster than the fluid and are flung outside the mixing region of the jet. This behavior is caused by the large-scale organized vortices, which capture the particles temporarily and fling them beyond the jet mixing region, giving rise to a lateral dispersion-rate which is higher than that of the shear-layer (Chung and Troutt, 1988).

To describe both from a qualitative and a quantitative viewpoint the selective dispersion associated with the large-scale vortices characteristic of the flow field under examination, we used particle Lagrangian tracking, choosing a set of particle sizes with characteristic time scales range similar to that of the coherent-structures (details are reported in Table 1). Specifically, we consider particle interactions with (i) vortex-rings (VR) and (ii) ribs; as a characteristic timescale, we choose the *turnover time* of the vortices (Campolo et al., 2004). The characteristic time of the vortex-rings is $\tau_{VR} \cong 1.69\tau$, nearly constant for each of those examined during our simulation. In the case of the ribs, which dimensions and turnover time change due to the stretching induced by the vortex-rings, we can determine only a time-scale range between $\tau_r \cong 0.25\tau$ and 1.0τ.

We tracked 4 swarms of 4×10^4 particles each, with diameters of 10, 20, 50 and 100 μm respectively. The distribution of particles in the inlet section is shown schematically in Fig. 1. Specifically, 2×10^4 particles, referred to as inner particles, are uniformly distributed at the inlet, in the inner circle of radius $r_m - \delta$, where δ is the boundary-layer thickness, whereas 2×10^4 particles, referred to as outer particles are uniformly distributed at the inlet in the outer ring defined by $r_m - \delta \leqslant r \leqslant r_m$. We decided to distribute particles in this non-uniform way first, because Lagrangian particle tracking is time-consuming and, in an effort to obtain more accurate statistics, we planned to have a larger number of particles in the region where the structures form, characterized by larger velocity gradients. The second reason is associated with the behavior of particles in a straight, turbulent pipe flow: particles tend to have higher concentration in the viscous sublayer (Reeks, 1983; Marchioli et al., 2003). We can thus anticipate that in real cases more particles will be found in inlet regions where the streamwise velocity is lower and characterized by larger velocity gradients. Particles initial velocity is set equal to the local fluid velocity.

3.6. Mechanisms of particle dispersion

In Fig. 11, the instantaneous azimuthal velocity in a cross-section of the diffuser is shown together with the position of the different size particles. The fingerprint of the rollers is clear in this frame. Fig. 11(a) and (b) are taken at time $t = 93.64\tau$, and Fig. 11(c) and (d) are taken at time $t = 96.36\tau$, at about one roller formation period after.

Chung and Troutt (1988) quantified the effect of the rollers in dispersing particles, and a similar mechanism was observed by Longmire and Eaton (1992) for particle dispersion in both forced and unforced jets. This action is clear in Fig. 11, in which the particle streaks follow the perturbation of the velocity field assuming a generally sinuous pattern. However, the different size particles behave differently. We should remember here that Fig. 11(c) and (d) are taken at nearly one roller formation period later—when the perturbation labeled A in Fig. 11(a) and (b) has evolved into the roller A in Fig. 11(c) and (d). This because larger particles, which leave the inlet pipe at a very small velocity, take longer to cover the same streamwise distance of smaller particles. We start from Fig. 11(d) and we observe that 100 μm particles, which have larger inertia, tend to "cut across" the roller. A similar behavior is observed for the 50 μm particles in Fig. 11(c) which, how-

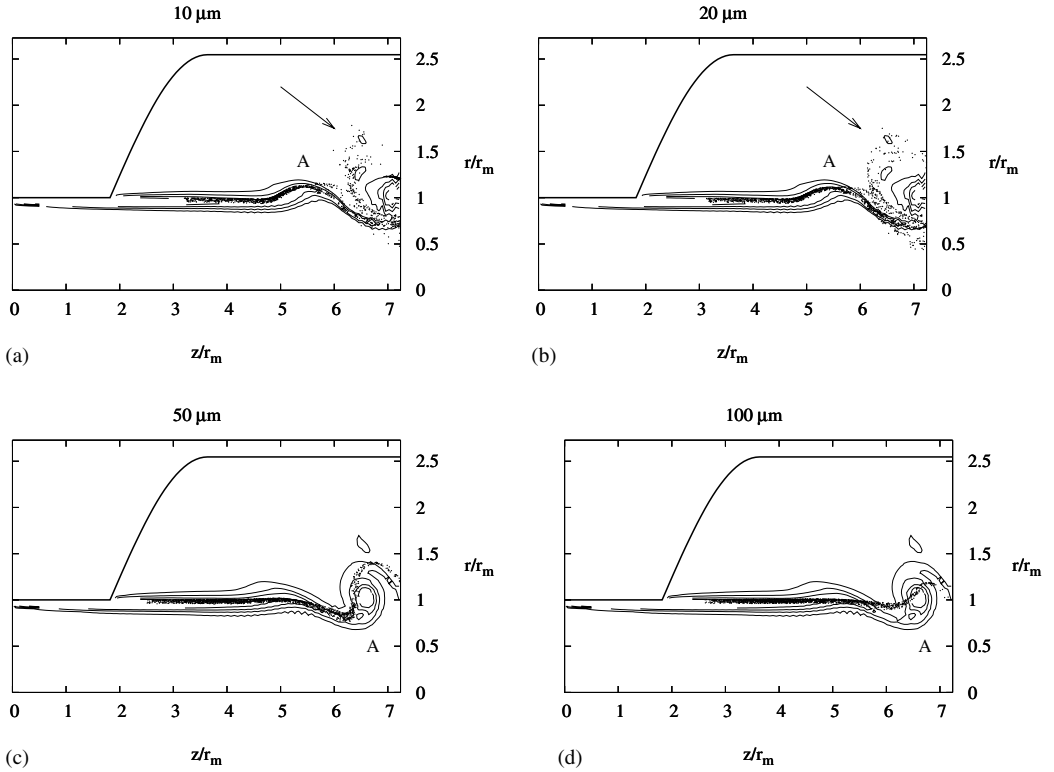

Fig. 11. Instantaneous section planes of azimuthal vorticity showing the evolution of the outer particle swarms and of a vortex ring (marked with A). Vorticity isocontours are used here to identify the position of the shear layer and of the ring vortex at a given instant. Snapshots are taken at $t = 93.64\tau$ for the 10 and 20 μm particles and at 96.36τ for the 50 and 100 μm.

ever, follow precisely the folding of the flow, being quicker to respond to sharp flow changes, and move around the external part of the rollers—indicated by the arrow.

A different behavior is observed for the smaller particles. Both 10 and 20 μm particles follow precisely the flow until they reach the external, upstream side of the roller. At this point, particles are driven into the outer flow as indicated by the arrow. This behavior has been first described by Longmire and Eaton (1992) who proposed a model for particle dispersion in the region outside the Kelvin–Helmholtz rollers. This mechanism is based on the sole action of the vortex-rings. Here, we observe that this drift is caused not only by the action of the azimuthal vorticity field but, for the smaller particles examined here, characterized by $St_{VR} \ll 1$, the action of a streamwise vorticity field characterizing the ribs becomes important. To examine in further detail this behavior, we use a three-dimensional view of the particle distribution at different times after the release, represented in Fig. 12. Here, only the distribution of the inner particles is shown. Location of the inlet boundary, of the exit of the inlet pipe and of the diffuser exit are indicated in figure. All inner particles, regardless of their size, are initially entrained by the core of the jet. At about $4r_m$ from the exit of the inlet pipe, that is the region where bursts and ribs start forming, the behavior of the smaller particles—10 and 20 μm—becomes different from that of the larger ones. It is interesting to observe that stronger differences are observed when the value of the particle-to-rib timescales ratio $St_r = \tau_p/\tau_r$ (i.e. the rib Stokes number, which values are reported in Table 1), is less than 1, according to the observations of Chung and Troutt (1988).

Particles entrained in the jet core (Fig. 12) follow it without visible radial and azimuthal motions, up to $4r_m$, where the passage in the central region of a vortex ring—characterized by a velocity lower than that of the jet core—causes a contraction of the swarm closer to the centreline, with a successive expansion. At the end of the expansion, the radial extent of the 50 and 100 μm particle swarms is the same we observed before the passage through the vortex (Fig. 12(c) and (d)). The same occurs for the downstream vortex rings, making these particles to follow the jet up to the diffuser exit without appreciable spreading. A different mechanism controls the motion of the smaller 10 and 20 μm particles which, after the contraction, expand in a wider region. In this case the ribs, the characteristic time-scale of which is similar to that of the particles, are able to capture these latter and to drive them outside the region of the vortex rings (i.e. the external limit of the shear layer). The phenomenon is emphasized for the 20 μm particles (Fig. 12(b)), which are not only driven but flung outside the region of the vortex rings, showing the highest radial dispersion-rate. This fact is confirmed by the snapshots in Fig. 12, which show that the dispersion for the 20 μm particles is larger than that of the smaller 10 μm—Fig. 12(a)—which in turn is larger that that of the 50 μm—Fig. 12(c)—and of the 100 μm particles—Fig. 12(d)—which tend to follow the motions of the jet core without spreading. In other words, the radial spreading rate of the swarm of particles can be maximum for a specific size of particles.

This tendency is more evident if we consider the outer particles (Fig. 13), which enter the diffuser in correspondence of the shear-layer and are thus entrained into a region characterized by larger velocity gradients. In Fig. 13, a snapshot of the four swarms of outer particles is shown; particle positions are taken at $t = 78.18\tau$ (above) and at 81.82τ (below). At approximately $4r_m$, the outer particles begin to interact with a vortex ring, as discussed in the case of inner particles, with an initial contraction of the swarm towards the centerline. The following expansion represents also in this case the event after which the differences in the behavior of particles with $St_r > 1$ and of particles with $St_r < 1$ become evident. Starting from the larger particles, we observe

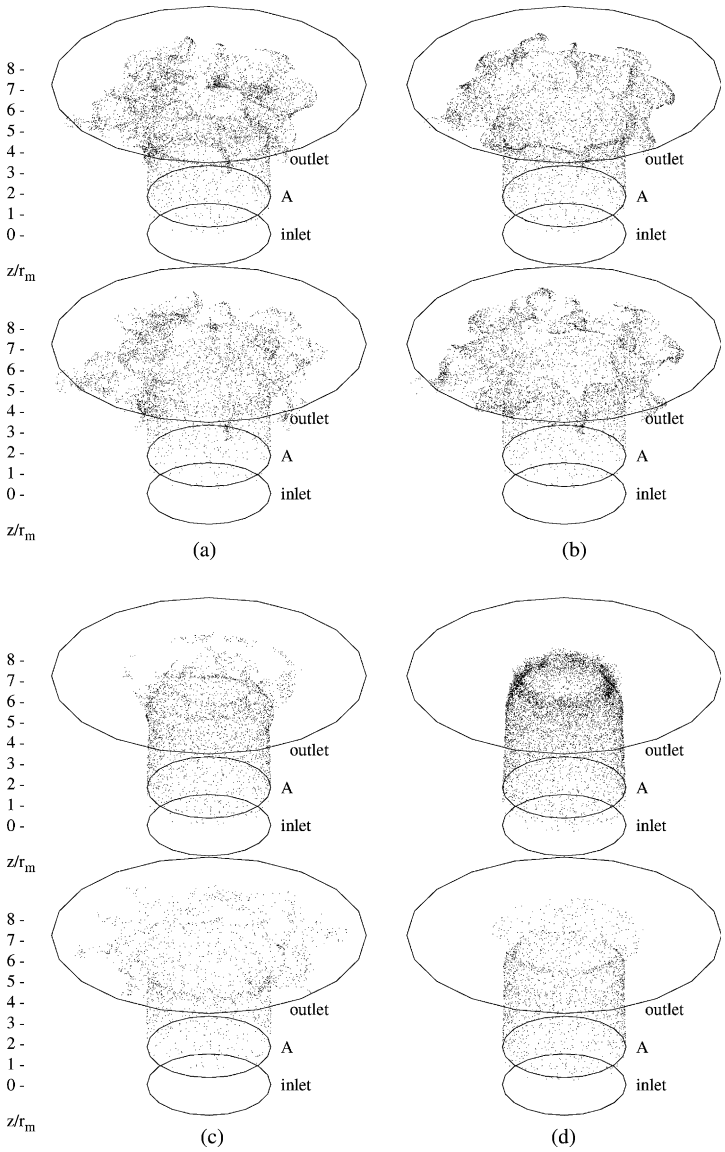

Fig. 12. Instantaneous position of the inner particle swarms, taken at time $t = 78.18\tau$ (above) and $t = 81.82\tau$ (below) from the release. The following particle sizes are represented: 10 μm (a), 20 μm (b), 50 μm (c) and 100 μm (d).

that their motion is dominated by the rollers. Particles sheet follows approximately the vorticity sheet which folds around the rollers. If we consider the set of the 50 μm particles, we can observe that their inertia is small enough to let them follow more precisely the boundary of the rollers and yet is large enough to drive them in the outer region, far enough from the action of the rollers and in the region of the ribs which are able to entrain a small fraction of the swarm.

As expected, the stronger interactions between particles and transitional structures occur for the 10 and 20 μm particles (Fig. 13(a) and (b)). After the contraction–expansion process caused

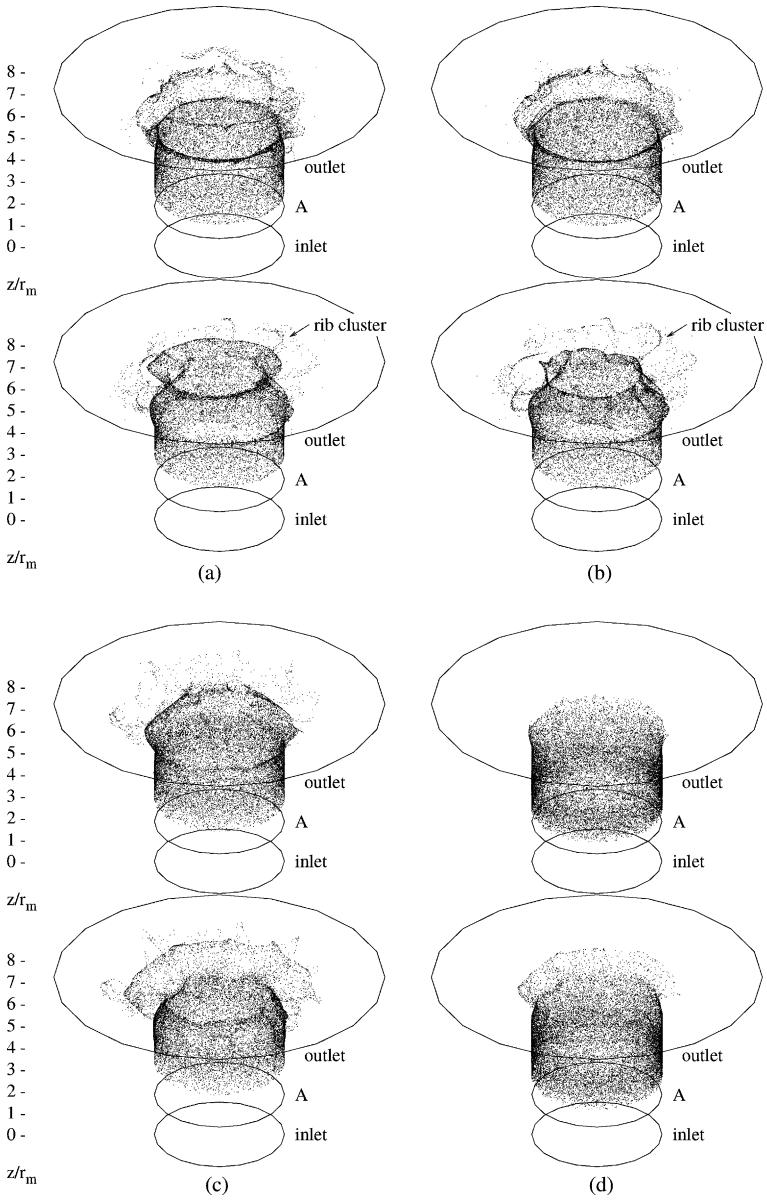

Fig. 13. Instantaneous position of the outer particle swarms, taken at time $t = 78.18\tau$ (above) and $t = 81.82\tau$ (below) from the release. The following particle sizes are represented: 10 μm (a), 20 μm (b), 50 μm (c) and 100 μm (d). Elongated particle clusters (rib clusters) are seen to form after the passage of a vortex-ring.

by the vortex ring, smaller particles do not follow around the toroidal vortex ring, but tend to migrate in the region of the bursts, slightly downstream, where they are captured by the bursts and driven outside by the stretched rib vortices. In this process, particles collect around the centerline of the bursts, forming elongated, quasi-streamwise clusters which we called *rib clusters*, shown in Fig. 13(a) and (b). The resulting distribution profile for the particles with $St_r < 1$

extends thus, in the radial direction, beyond the shear layer region with an azimuthally irregular (and, by observing Fig. 13(b) we can anticipate that it is azimuthally periodic) concentration.

3.7. Mechanisms of particle preferential distribution

Particle penetration and related dispersion effects are only one aspect of the interaction between particles and jet structures. It is useful to define also an integral parameter to characterize quantitatively the degree of particle segregation. Specifically, in different flow configurations, quasi-pure advection (Soldati, 2000) was observed for particle time scale very small compared to the flow structures time scale, whereas segregation and preferential accumulation has been observed when the timescale of particles becomes comparable to that of the flow structures (Campolo et al., 2004).

Maxey (1987) and Squires and Eaton (1990) found that the concentration of inertial particles in a turbulent flow correlates well with the strain-rate and the vorticity fields. In particular, Squires and Eaton (1990) studied the effect of turbulence on particle concentration in an isotropic turbulent flow using DNS, and observed that inertial particles collect preferentially in regions of low vorticity and high strain-rate, this effect decreasing for increasing particle inertia. The second invariant of the velocity gradient tensor (VGT) $Q = \mathrm{II}_{\mathrm{VGT}}$, defined in Eq. (11), is an adequate tool to identify regions of simultaneous high strain-rate and low vorticity, and *vice versa*, being the difference between a scalar function of the strain-rate tensor S_{ij}—the symmetric part of the VGT—and a scalar function of the vorticity tensor Ω_{ij}—the antisymmetric part of the VGT. We will thus use Q as a macroscopic indicator of particle preferential distribution to quantify, from a statistical viewpoint, the tendency of particles to segregate in correspondence of the ribs.

Observing again Fig. 8, an isosurface of large positive Q shows the instantaneous position of bursts and rib vortices, which are thus characterized by high strain-rate and low vorticity. In such regions, following the criterion of Squires and Eaton (1990), we expect to find higher particle concentrations. From a qualitative viewpoint, we already observed particle clustering inbetween the rib pair in Fig. 13.

Clearly, a certain amount of particles lies, for a given instant, in regions where no structures are observed, i.e. where the value of Q^*, due to the presence of both a low-vorticity and a low-strain value, is closer to 0. This results in the presence of a further peak centered at $Q^* = 0$, with a height proportional to the percentage of particles not entrained by the flow structures.

In Fig. 14 we show the PDF of the instantaneous particle concentration number as a function of Q (non-dimensionalized through the characteristic flow timescale defined in Eq. (1), i.e. $Q^* = \tau^2 Q$) calculated for the four swarms of outer particles at time $t = 90.91\tau$. Each PDF is characterized by a high peak centered at $Q^* = 0$. According to the classification of Chong et al. (1990), the value $Q^* = 0$ indicates regions characterized by absence of flow structures, which are thus preferentially sampled by particles. The PDF, however, is also characterized by a second, smaller peak shifted towards values of positive Q^*. This peak is well defined for the smaller particles, is weak for the 50 μm particles and is apparently absent in the PDF of the largest particles. The presence of the secondary peak indicates that particles preferentially sample regions characterized by high strain and low vorticity, which are indeed the fingerprints of the rib-pair and burst structures as shown in Fig. 8.

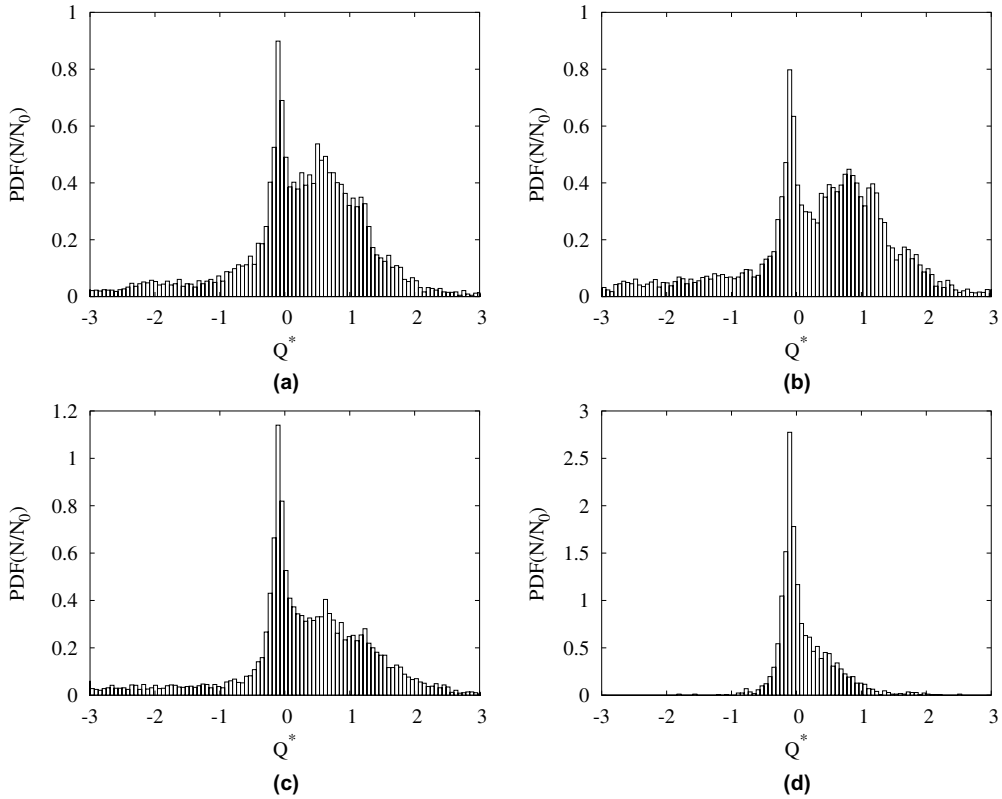

Fig. 14. PDF of the outer-particles concentration number N/N_0 calculated as a function of the second-invariant of the VGT at time 90.91τ. Smaller particles of 10 μm (a) and 20 μm (b) show to migrate preferentially in regions of positive Q. This tendency decays as the particle inertia increases, as it is visible for the 50 μm (c) and especially for the 100 μm particles (d).

Statistics shown in Fig. 14 are calculated at time $t = 90.91\tau$. We calculate the same statistics for a large number of different instants and we obtained no significant difference suggesting that the behavior of the particles is maintained during the entire observation time window.

Since particle distribution—at least for the three smaller sizes—correlates well with the position of the rib pairs, we anticipate a periodicity along θ of the particle rib clusters.

In Fig. 15, we explore the correspondence of the space frequency of the rib-clusters of particles and the space frequency of the pairs of rib vortices. By Eq. (12), we introduced the wavenumber spectrum to characterize the spatial periodicity of the azimuthal velocity cross-correlation $C_{uu}(\theta)$ in order to determine the spatial periodicity of the bursts within $\theta = 0$ and $\theta = 2\pi$. Using this definition, we found that the statistically most probable number of simultaneous bursts in our flow configuration is close to 8 (see Fig. 10). In the same way, we calculate the wavenumber spectrum of the 20 μm outer-particle concentration number $N/N_0(\theta)$ measured at $z/r_m = 5.45$ and averaged over the time window of the Lagrangian tracking. The result is shown in Fig. 15(a), where a peak centered at $v_b = 8$, indicated by the dash-dot line is shown. In Fig. 15(b) we show the wavenumber spectrum of the time-averaged radial velocity component $\overline{u_r(\theta)}$. This shows, together with the higher peak observed in correspondence to $v_b = 7.5$ (close to 8), two other secondary peaks, lo-

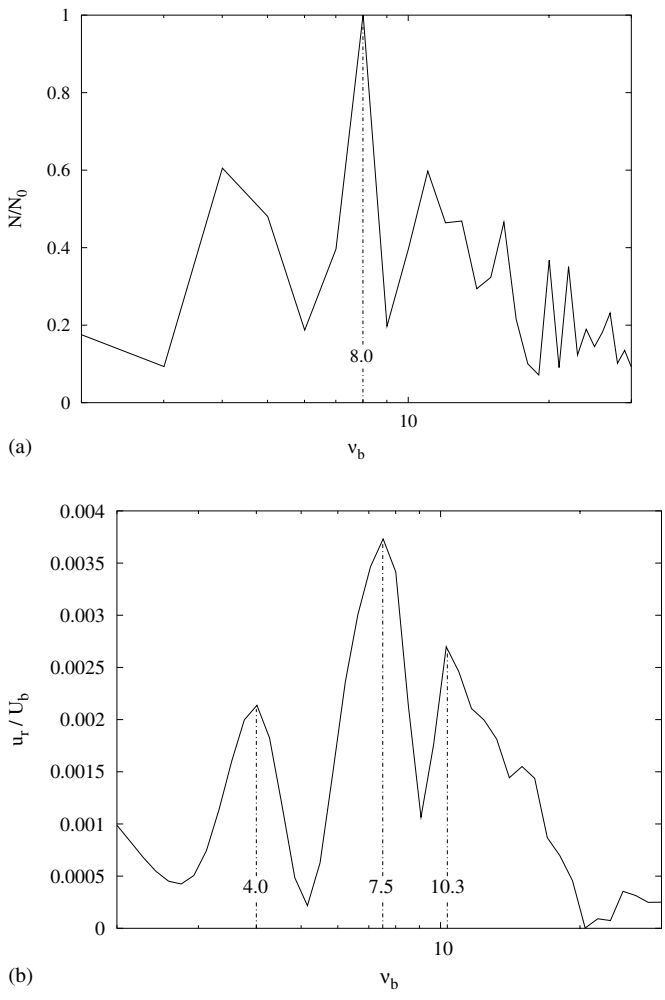

Fig. 15. Azimuthal periodicity of the normalized particle concentration number (a) and of the time-averaged radial velocity of the fluid (b) at $z/r_m = 5.45$, plotted as a function of the wavenumber ν_b, i.e. the number of events registered for θ ranging from 0 to 2π (describing a complete rotation around the jet axis). The two curves are strictly correlated and the higher periodicity is nearly the same we found for the bursts, we evaluated by means of the wavenumber spectra of Fig. 10.

cated respectively at $\nu_b = 4.0$ and at $\nu_b = 10.3$ which are very similar to those observed in the concentration wavenumber spectrum of Fig. 15(a), thus confirming the close correspondence between the radial fluid motions and the radial dispersion of the inertial particles with $St_r < 1$.

4. Conclusions and further development

In this work, we examined the structure of the flow field and the mechanisms of dispersion for inertial particles in the near-field of a large-angle, axisymmetric diffuser used to connect two cir-

cular ducts of different diameters. This type of configuration is found in a variety of industrial applications, such as hydraulic plants, dust filtering facilities and automotive exhaust systems. The specific geometry analyzed is an idealized version of the diffuser used to connect the exhaust duct of a Diesel engine with the chamber containing the soot abatement filter.

To simulate the time-dependent, turbulent flow field, we used a finite-difference and Fourier expansion LES code, written to solve the Navier–Stokes equations in a cylindrical reference frame. The code uses the immersed-boundaries approach (Fadlun et al., 2000) to model the walls with complex shape, such as the pipe-diameter variations and the curved profile of the diffuser. A constant, logarithmic velocity profile is imposed at the inlet of the domain, whereas the convective-outlet boundary condition is applied to the outlet.

We focused first on the boundary-layer separation leading to the formation of a shear-layer in the downstream duct. Comparisons with benchmark cases of boundary-layer separation such as the backward-facing step, the planar jet and the circular jet showed that the flow analyzed reproduces many features of the axisymmetric jets, with a small recirculation effect in the region outside the shear-layer (outer region) due to the presence of the walls of the downstream, larger pipe.

A Kelvin–Helmholtz instability of the shear-layer is responsible for the formation of large-coherent annular rollers, or vortex-rings (VR), shed with a nearly fixed frequency and grow in dimensions from one diameter downstream the separation point up to the domain outlet. During this growing stage, a wave deformation of the core of these vortices, also observed in earlier works (Yule, 1978) causes the formation of secondary, streamwise structures, observed in planar jets, known as *ribs*, and of outward directed, radial jets of fluid inbetween two successive VR, called *bursts*.

Observations on the behavior of the dispersion of inertial particles (with diameter of 10, 20, 50 and 100 μm and particle-to-fluid density ratio $\rho_p/\rho = O(10^3)$)—simulated by means of Lagrangian tracking with one-way coupling momentum transfer between fluid and particles—demonstrate that the spreading-rate of these particles is strongly affected by their Stokes number $St = \tau_p/\tau_f$. We found that particles with $St < 1$ (calculated considering the circulation time of the vortices as a fluid characteristic time) are captured by the structures and entrained in the mixing region of the jet, spreading with the same spreading-rate of these latter. This behavior is emphasized when $St = 1$, but the tendency rapidly drops for $St > 1$, as observed by Chung and Troutt (1988).

In this work, we completed the experimental observations by Longmire and Eaton (1992) who observed particle clustering between vortex ring structures and proposed a mechanism based on the action of these latter to explain ejection of particles in the outer region. We find that this phenomenon is caused not only by the action of the azimuthal vorticity field but, for particles characterized by $St_{VR} \ll 1$ (see Table 1) the action of the streamwise vorticity field characterizing the ribs becomes important. The identification of the burst ejections as regions of high strain-rate and low vorticity, together with the tendency of inertial particles to collect in similar regions, first observed in the work of Squires and Eaton (1990) and verified here for the lighter particles, suggest that the particles of 10 and 20 μm follow the bursts and are convected in the outer region, collecting in clusters having the same shape and spatial distribution of the fluid structures, specifically of the rib vortices; thus, we called them *rib clusters*. The spatial distribution of the rib clusters is qualitatively similar to that of the bursts, and this correspondence is confirmed if we compare the wavenumber (spatial) spectrum of the time-averaged particle concentration number N/N_0 and the wavenumber spectrum of the time-averaged radial velocity $\overline{u_r(\theta)}$.

The local, non-stationary flow field due to the presence of coherent structures grown as the effect of instabilities in the shear-layer of a (confined) round jet, can be thus considered one of the most important mechanisms leading to particle dispersion in this type of flow configuration, but the effect of such motions rapidly decreases for increasing particle Stokes number.

Finally, there is some evidence in the literature that flow structures may be modified by flow field modulation. This introduces a further possibility for dispersion control in which the flow field modulation is tuned to generate flow structures having specific characteristic time scale. Promising results have been obtained in simple flow configuration (see Lazaro and Lasheras, 1992 among others) and further analyses are required to extend these results to the round jet. These will be the object of future numerical investigations.

Acknowledgments

The support to this work supplied by the "Centro Ricerche FIAT" of Orbassano (TO, Italy) is gratefully acknowledged.

First author (FS) gratefully acknowledges the grant support from ATA (Associazione Tecnica dell'Automobile) of Orbassano (Italy).

References

Ahmed, A.M., Elghobashi, S., 2001. Direct numerical simulation of particle dispersion in homogeneous turbulent shear flows. Phys. Fluids 13, 3346–3364.

Akselvoll, K., Moin, P., 1996. Large-eddy simulation of turbulent confined coannular jets. J. Fluid Mech. 315, 387–411.

Anderson, S.L., Longmire, E.K., 1995. Particle motion in the stagnation zone of an impinging air jet. J. Fluid Mech. 299, 333–366.

Apte, S.V., Mahesh, K., Moin, P., Oefelein, J.C., 2003. Large-eddy simulation of swirling particle-laden flows in a coaxial jet combustor. Int. J. Multiphase Flow 29, 1311–1331.

Armenio, V., Fiorotto, V., 2001. The importance of the forces acting on particles in turbulent flows. Phys. Fluids 8, 2437.

Bernal, L.P., Roshko, A., 1986. Streamwise vortex structure in plane mixing layers. J. Fluid Mech. 170, 499–525.

Bradshaw, P., Ferriss, D.H., Johnson, R.F., 1964. Turbulence in the noise-producing region of a circular jet. J. Fluid Mech. 19, 591–624.

Campolo, M., Salvetti, M.V., Soldati, A., 2004. Mechanisms for microparticle dispersion in a jet in crossflow. AIChE J., 50.

Cerbelli, S., Giusti, A., Soldati, A., 2001. ADE approach to predicting dispersion of heavy particles in wall-bounded turbulence. Int. J. Multiphase Flow 27, 1861–1879.

Chein, R., Chung, J.N., 1988. Simulation of particle dispersion in a two-dimensional mixing layer. AIChE J. 34, 946–954.

Chong, M.S., Perry, A., Cantwell, B.J., 1990. A general classification of three dimensional flow fields. Phys. Fluids A 2, 765–777.

Chung, J.N., Troutt, T.R., 1988. Simulation of particle dispersion in an axisymmetric jet. J. Fluid Mech. 186, 199–222.

Crowe, C.T., Chung, J.N., Troutt, T.R., 1989. Particle mixing in free shear flows. Progr. Energy Combust. Sci. 14, 171–194.

Crowe, C., Sommerfeld, M., Tsuji, Y., 1998. Multiphase Flows with Droplets and Particles. CRC Press, Boca Raton, FL.

da Silva, C.B., Métais, O., 2002. On the influence of coherent structures upon interscale interactions in turbulent plane jets. J. Fluid Mech. 473, 103–145.

Davies, P.O.A.L., Fisher, M.J., Barratt, M.J., 1963. The characteristic of the turbulence in the mixing region of a round jet. J. Fluid Mech. 15, 337–367.

Eaton, J.K., Fessler, J.R., 1994. Preferential concentration of particles by turbulence. Int. J. Multiphase Flow 20, 169–209.

Fadlun, E.A., Verzicco, R., Orlandi, P., Mohd-Yusof, J., 2000. Combined immersed-boundary/finite-difference methods for three-dimensional complex flow simulations. J. Comp. Phys. 161, 35–60.

Germano, M., Piomelli, U., Moin, P., Cabot, W.H., 1991. A dynamic subgrid-scale eddy viscosity model. Phys. Fluids 3, 1760–1765.

Gutmark, E., Ho, C.-M., 1983. Preferred modes and the spreading rates of jets. Phys. Fluids 26, 2932–2938.

Hussain, A.K.M.F., Tatsumi, T. (Eds.), 1983. Turbulence and Chaotic Phenomena in Fluids. North-Holland, p. 453.

Hussain, A.K.M.F., 1986. Coherent structures and turbulence. J. Fluid Mech. 173, 303–356.

Hussain, A.K.M.F., Clark, A.R., 1981. On the coherent structure of the axisymmetric mixing layer: a flow-visualization study. J. Fluid Mech. 104, 263–294.

Kaltenbach, H.-J., Fatica, M., Mittal, R., Lund, T.S., Moin, P., 1999. Study of flow in a planar asymmetric diffuser using large-eddy simulation. J. Fluid Mech. 390, 151–185.

Klaassen, G.P., Peltier, W.R., 1989. The role of transverse secondary instabilities in the evolution of free shear layers. J. Fluid Mech. 202, 367–402.

Lazaro, B.J., Lasheras, J.C., 1992. Particle dispersion in the developing free shear layer. Part I. The natural flow. J. Fluid Mech. 235, 143–178.

Le, H., Moin, P., Kim, J., 1997. Direct numerical simulation of turbulent flow over a backward-facing step. J. Fluid Mech. 330, 349–374.

Lee, S., Lele, K., Moin, P., 1992. Simulation of spatially evolving turbulence and the applicability of Taylor's hypothesis in compressible flow. Phys. Fluids A 4 (7), 1521–1530.

Longmire, E.K., Eaton, J.K., 1992. Structure of a particle-laden round jet. J. Fluid Mech. 236, 217–257.

Loth, E., 2000. Numerical approaches for motion of dispersed particles, droplets and bubbles. Prog. Energy Combust. Sci. 26, 161–223.

Lowery, P.S., Reynolds, W.C., 1986. Numerical simulation of a spatially-developing, forced, plane mixing layer. Rep. TF-26, Thermosciences Division, Department of Mechanical Engineering, Stanford University.

Marchioli, C., Soldati, A., 2002. Mechanisms for particle transfer and segregation in turbulent boundary layer. J. Fluid Mech. 468, 283–315.

Marchioli, C., Giusti, A., Salvetti, M.V., Soldati, A., 2003. Direct numerical simulation of particle wall transfer and deposition in upward turbulent pipe flow. Int. J. Multiphase Flow 29, 1017–1038.

Marcu, B., Meiburg, E., 1996. Three-dimensional features of particle dispersion in a nominally plane mixing layer. Phys. Fluids 8, 2266–2268.

Maxey, M.R., 1987. The gravitational settling of aerosol particles in homogeneous turbulence and random flow fields. J. Fluid Mech. 174, 441–465.

Maxey, M.R., Riley, J.J., 1983. Equation of motion for a small rigid sphere in a nonuniform flow. Phys. Fluids 26, 883–889.

Na, Y., Moin, P., 1998. Direct numerical simulation of a separated turbulent boundary layer. J. Fluid Mech. 370, 175–202.

Pauley, L.L., Moin, P., Reynolds, W.C., 1988. A numerical study of unsteady laminar boundary layer separation. Rep. TF-34, Thermosciences Division, Department of Mechanical Engineering, Stanford University.

Reeks, M., 1983. The transport of discrete particles in inhomogeneous turbulence. J. Aerosol Sci. 14, 729–739.

Rowe, P.N., Enwood, G.A., 1962. Drag forces in hydraulic model of a fluidized bed—Part I. Trans. Inst. Chem. Engrs. 39, 43–47.

Schlichting, H., 1979. Boundary-layer Theory, seventh ed. McGraw-Hill.

Soldati, A., 2000. On the effects of electrohydrodynamic flows and turbulence on aerosol transport and collection in wire-plate electrostatic precipitators. J. Aerosol Sci. 31, 293–305.

Squires, K.D., Eaton, J.K., 1990. Preferential concentrations of particles by turbulence. Phys. Fluids A 3, 1169–1178.

Stanley, S.A., Sarkar, S., Mellado, J.P., 2002. A study of the flow-field evolution and mixing in a planar turbulent jet using direct numerical simulation. J. Fluid Mech. 450, 377–407.

Tang, L., Wen, F., Yang, Y., Crowe, C.T., Chung, J.N., Troutt, T.R., 1992. Self-organizing particle dispersion mechanism in a plane wake. Phys. Fluids 4, 2244–2251.

Verzicco, R., Orlandi, P., 1996. A finite-difference scheme for the three-dimensional incompressible flows in cylindrical coordinates. J. Comp. Phys. 123, 402.

Verzicco, R., Mohd-Yusof, J., Orlandi, P., Haworth, D., 2000. Large-eddy simulation in complex geometric configurations using boundary body forces. AIAA J. 38, 427–433.

Wen, F., Kamalu, N., Chung, N.J., Crowe, C.T., Troutt, T.R., 1992. Particle dispersion by vortex structures in plane mixing layers. J. Fluid Eng. ASME Trans. 114, 657–666.

Yang, Y., Crowe, C.T., Chung, J.N., Troutt, T.R., 2000. Experiments on particle dispersion in a plane wake. Int. J. Multiphase Flow 26, 1583–1607.

Yule, A.J., 1978. Large-scale structures in the mixing layer of a round jet. J. Fluid Mech. 89, 413–432.